Title: Untethered unidirectionally crawling gels driven by an asymmetry in contact forces

Authors: A. Pantula, [†] B. Datta, [‡] Y. Shi, [‡] M. Wang, [†] J. Liu, [‡] S. Deng, [‡] N. J. Cowan, [‡¶] T. D. Nguyen, [‡§] D. H. Gracias [§#††‡‡§§†*]

Affiliations:

[†] Department of Chemical and Biomolecular Engineering, Johns Hopkins University; Baltimore, MD 21218, USA.

[‡] Department of Mechanical Engineering, Johns Hopkins University; Baltimore, MD 21218, USA.

[§] Department of Materials Science and Engineering, Johns Hopkins University; Baltimore, MD 21218, USA.

[¶] Laboratory for Computational Sensing and Robotics (LCSR), Johns Hopkins University; Baltimore, MD 21218, USA.

[#] Department of Chemistry, Johns Hopkins University; Baltimore, MD 21218, USA

[††] Department of Oncology, Johns Hopkins School of Medicine; Baltimore, MD 21205, USA.

[‡‡] Sidney Kimmel Comprehensive Cancer Center, Johns Hopkins School of Medicine; Baltimore, MD 21205, USA.

[§§] Hopkins Extreme Materials Institute, Johns Hopkins University; Baltimore, MD 21218, USA.

*Email: dgracias@jhu.edu

Abstract:

The development of untethered soft robots capable of locomotion in response to environmental stimuli is important for biomimetics, drug delivery, and non-minimally invasive surgery. Reversible thermoresponsive hydrogels, which swell and shrink in the temperature range of (30-60 °C), provide an attractive material class for operating such untethered soft robots in human physiological and ambient conditions. Crawling has been demonstrated previously with thermoresponsive hydrogels but needs a patterned or ratcheted surface to break symmetry for unidirectional motion. Here, we demonstrate a new locomotor mechanism for unidirectionally crawling gels driven by spontaneous asymmetries in contact forces during swelling and deswelling of segmented active thermoresponsive poly (N-isopropyl acrylamide) (pNIPAM) and passive polyacrylamide (pAAM) bilayers with suspended linkers. Experiments demonstrate consistent unidirectional movement of hydrogel crawlers across multiple thermal cycles on flat, unpatterned surfaces. We explain the mechanism using finite element simulations and varying experimental parameters such as the number of segments, linker size, and design. We compare and validate experiments, image analysis, and models to elucidate design and engineering principles. We anticipate that this mechanism could be widely applied and adapted to create a variety of shape-changing and smart locomotors.

One-Sentence Summary:

By manipulating the geometry and number of bilayer segments of a multisegmented gel robot, we generate asymmetric contact forces to realize unidirectional crawling on an unpatterned surface over multiple thermal stimulation cycles.

INTRODUCTION

Stimuli-responsive, untethered, soft robots that can locomote in aqueous environments can have important biomedical applications. (1–3) Compared to tethered robots that utilize fluidic or pneumatic signals to control their motion, untethered robots are mass-producible, maneuverable in tight spaces, and do not require wiring or external power sources. (4) Stimuli-responsive hydrogels, which can undergo volumetric phase transitions in response to stimuli such as heat, light, pH, biochemicals, electric, and magnetic fields are attractive materials for structuring untethered robots. (3–8)

Previously, researchers have used hydrogels to create a range of shape changes and transformer hydrogels such as grippers, fluidic actuators, and valves. (3, 9–11) An important class of stimuli-responsive hydrogels is reversibly-thermoresponsive poly(N-isopropylacrylamide) (pNIPAM). These hydrogels undergo tunable lower critical solution temperature (LCST) transitions in the human physiological and ambient temperatures up to 50 °C. LCST transitions of these polymers can be tuned by varying molecular and blending with compatible copolymers or mixing with ionic liquids. (12, 13)

Researchers have utilized various techniques, including molding, 3D printing, and stereolithography, to create micro and mesostructured pNIPAM structures, including those capable of locomotion. For example, Maeda *et al.* used the Belousov–Zhabotinsky (BZ) oscillatory reaction for differential swelling as an actuation mechanism at a constant temperature. (14) Elsewhere, researchers have used these stimuli-responsive hydrogel bilayers to create a variety of crawling mechanisms. (15–19) However, it is challenging to break symmetry (a fundamental

requirement of directed locomotion) using swelling and deswelling cycles as needed for directed locomotion. Consequently, previous attempts at creating bilayer hydrogel crawlers have utilized patterned substrates on ratcheted surfaces or constrained channels to break symmetry and direct motion, limiting these robots' applicability. Also, prior work has relied on inherently simple single-segment bilayer designs, often limited by fabrication processes. (*19*)

Here, we describe how we can use systematic and asynchronous changes in robot morphology, driven by varying temporal swelling and deswelling of connected gel segments, to break the spatial (fore-aft) symmetry of contact forces and direct motion on flat surfaces without needing constrained environments or ratcheted substrates. Remarkably, as we show, symmetry is spontaneously broken due to asymmetries in contact surface forces caused by the structural design of the robot. Our innovation involves three new principles, (a) The use of gel segments of different thicknesses and lateral dimensions to induce spatiotemporal asymmetries in swelling and deswelling, (b) the use of a suspended linker with different stiffness and patterns to study the parameters that influence robot displacement, and (c) varying experimental parameters like the number of bilayer segments and linker pattern to the dependence of robot actuation. We fabricated our robots by direct ink writing (DIW), a 4D printing technique that uses pressure-based extrusion for layer-by-layer assembly of multiple materials and characterized them over multiple heating and cooling cycles. We also simulated the thermo-chemo-mechanical behavior of the hydrogel robots using finite element analysis to investigate the mechanism of locomotion. Our studies suggest a mechanism for designing a new class of untethered stimulus-responsive locomotors, and our approach that leverages 3D printing and simulations provides significant tunability, scalability, and versatility. (*10*, *20–28*)

DESIGN AND FABRICATION OF MULTISEGMENTED BILAYER GEL ROBOTS

Crawling via cycles of musculoskeletal traveling waves—i.e., kinematic and dynamic phase differences along a fore-aft body axis—provides a common and effective means of locomotion for various organisms as a combination of nervous signals, musculoskeletal deformation, and environmental factors and indeed many biological locomoting systems, such as inchworms and snakes, exhibit traveling waves along their bodies to produce motion; (*29, 30–36*). Here, we propose a new strategy that exploits the geometry of actuators by engineering morphological asymmetries in lateral dimensions and thickness of bilayers to generate the requisite fore-aft phase differences during swelling deswelling without the need to use independent stimuli. We do this by designing morphological gradients along the fore-aft axis of the soft robotic chassis; these gradients in morphology lead to a gradient in actuator dynamics, ultimately instantiating a wave-like locomotor gait that only requires a single input.
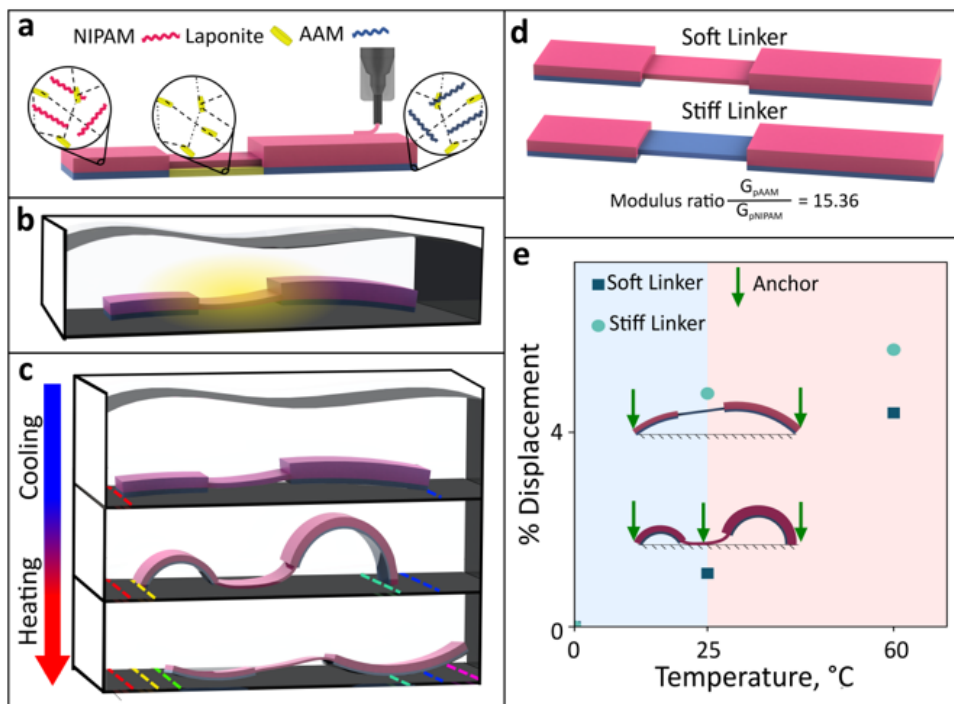
Figure 1. Fabrication and design of multisegmented robots with the linker. (a) 3D printing process, **(b)** Sacrificial layer dissolution, and **(c)** Thermal actuation. **(d)** Variation of linker morphology **(e)** Thermal cycling of robot and varying the contact force distribution to increase robot actuation distance. The area shaded blue describes the cooling half-cycle and red the heating half-cycle.

We designed multisegmented robots with two bilayers of different morphology connected by a linker (**Figure 1**). The bilayers are composed of a thermally responsive swelling gel (active material) and a non-swelling gel (passive material). We used a thermoresponsive monomer N-isopropylacrylamide (NIPAM) with a lower critical solution temperature (LCST) of 32 °C as our active ink and acrylamide (AAM) for our passive ink. We modified our monomer inks to enable direct ink writing, an extrusion-based 3D printing technique for shear-thinning gel inks. Our inks were monomer dispersions in water mixed with Laponite® (nano-clay rheological modifier) and crosslinked the mixture after printing by UV exposure. (*28, 37*) One key innovation central to symmetry breaking is a suspended central linker that connects the bilayer segments. We developed a sacrificial ink composed of a pure Laponite® aqueous solution that supports a second gel layer during fabrication. We subsequently dissolved this sacrificial layer to create the suspended linker. Since Laponite® does not crosslink during UV curing, the layer dissolves readily when the active layer swells (**Figure 1b).** We utilized a two-nozzle printer and switched one of our inks out of the printer head during the fabrication to allow printing with our third ink. For this, we had to control the print path precisely, particularly the order we printed the different segments in layer 1, to give us enough time to conduct the switch. We started with AAM and sacrificial inks in the two printer heads and printed the sacrificial layer first. Then, while the printer was using the printer head with AAM, we switched the sacrificial ink with NIPAM. We used the same nozzle which we cleaned during the print for the two swapped inks to ensure no misalignment.
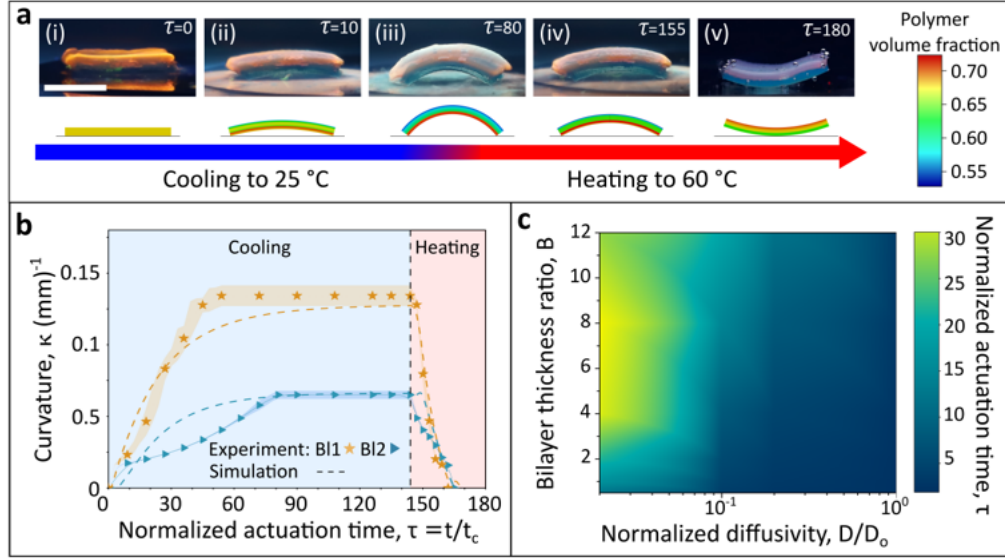
Figure 2. Tuning actuation time and curvature of bilayers by varying thickness ratio during thermal cycling. (a) Experimental images and simulation snapshots of the bending of the 0.8 mm pNIPAM-0.4 mm pAAM bilayer with respect to normalized actuation time (τ=t/t_c of bilayers (t_c=(l_c^2)/D_o, l_c=1 mm; D_o=5×10^{-9} m^2/s) taken during one thermal cycle of cooling at 25 °C **(i-iii)** *and heating* at 60 °C **(iv-v)** 80. Both bilayers fully swell by *(iii)* τ = 80. The bilayers deswell beyond their cured state and achieve negative curvature by the end of heating **(v)** τ =160. Scale bar indicates 10mm, and the color legend indicates the polymer volume fraction from simulations; smaller numbers indicate more swelling. The polymer volume fractions at cured state, fully swollen at 25 °C, and fully deswollen state are 0.67, 0.59, and 0.72, respectively. **(b)** Radius of curvature of the 0.8 mm pNIPAM-0.4 mm pAAM bilayer (**Bl1**) and 0.8 mm pNIPAM-0.8 mm pAAM bilayer (**Bl2**) observed over normalized actuation time for cooling (blue area) and heating (red area) half-cycles compared to the fitted model. Shading along each experimental plot represents a standard deviation with a sample size of three. **(c)** Normalized actuation time by varying thickness ratio, B=h_{pNIPAM}/h_{pAAM}, and normalized permeability, D/D$_o$. The black dots indicate the experimental parameters used for the fabrication: More details about experiments on other bilayers, modeling, the parameters used, and graphs are in the Supporting Information.

After printing, we cured and crosslinked the robot for 200 s at 0.4 W/cm^2, holding our probes approximately 3 cm from the structure. After curing, we swelled our robot at room temperature to dissolve the sacrificial ink and set it up for actuation tests. We investigated the response of multiple robots while changing linker morphology and the number of segments to understand the influence of different engineering parameters on the morphology and displacement of the robots (**Figure 1c-e).**

RESULTS

The swelling and deswelling rate of bilayers can be tuned

We first characterized the transient swelling-induced bending behavior of rectangular bilayers with varying dimensions over a thermal cycle (heating and cooling half-cycles) by measuring the curvature. We used 10 mm ×15 mm rectangular bilayers with two thicknesses of the pAAM layer (0.4 mm, 0.8 mm) and four thicknesses of the pNIPAM layer (0.4 mm, 0.8 mm, 1.2 mm, and 1.6 mm).

We plotted the radius of curvature of our bilayers during the heating and cooling cycle against normalized time $\tau = t/t_c$ where $t_c = l_c^2/D_o$, l_c=1 mm; D_o=5×10^{-9} m^2/s. Our thinnest bilayer, 0.4 mm pNIPAm-0.4 mm pAAM, equilibrated the fastest with the highest curvature during the cooling cycle, followed by the 0.8 mm pNIPAM-0.4 mm pAAM bilayer. The thicker bilayers with (0.8 mm, 1.2 mm, 1.6 mm) pNIPAM and 0.8 mm pAAM equilibrated in similar time ranges and curvatures, 1.6 mm pNIPAM bilayer having the smallest curvature (**Figure 2 a, b and Fig S2**). We observed that during the cooling half-cycle, swelling time varied widely from (τ =50-110) for different bilayers. This variation is due to the bilayers with thicker pNIPAM taking longer to achieve equilibrium swelling. During the heating half-cycle, the bilayers deswelled twice as fast (τ =150-180). (*38*) We summarize the thermal cycling data on the rest of the bilayers in **Fig. S2**.

We applied finite element analysis (FEA) of the swelling and deswelling induced transient bending of the bilayers to determine the swelling and deswelling properties of the hydrogels (**Table S1**). We described the rapid deswelling of pNIPAM by modifying the constitutive model to include two different diffusivities for the swelling and deswelling process. Details of the finite element simulations and procedure for parameter calibration are in the **SI**. We next applied FEA to investigate the effects of material and geometric properties of the bilayer on the actuation time,

defined as the time required to reach 63.2% of the equilibrium bending curvature (**Figure 2c**). The actuation time was most sensitive to the diffusivity of the pNIPAM and the bilayer thickness ratio. Bilayers with a smaller thickness ratio and a larger diffusivity for the active material produce shorter actuation times.

Robot actuation-two-segment robot with a flexible pNIPAM linker

We utilized the characterization data from the thermal cycling of the various pNIPAM-pAAM bilayers and the model parameters to design multisegmented gels with asymmetries in contact forces. We used a smaller (0.8 mm pNIPAM-0.4 mm pAAM) bilayer and a larger (1.2 mm pNIPAM-0.4 mm pAAM) bilayer connected by a suspended pNIPAM linker. Geometric details on all our robots are in **Fig. S4-6**. After curing and sacrificial structure dissolution, we thermally cycled the robot in water by switching the temperature to 60 °C for the heating half-cycle and 25 °C for the cooling half-cycle.

During the cooling half-cycle, the robot was allowed to swell at room temperature. We observed that the mismatch in swelling properties and thickness ratio of active and passive hydrogel in bilayers caused swelling-induced bending in both bilayer segments, which resulted in forward translation of the robot. The two bilayers had different curvatures, with the thinner bilayer having a higher curvature. The flexible linker swelled and sagged to touch the underlying surface along with the outer edge of both the bilayers. Once we switched the actuation cycle to heating, the robot recovered from the swollen-bent state rapidly because of the faster deswelling kinetics of the active hydrogel. Further heating resulted in pNIPAM deswelling beyond its cured state length and caused the bilayers to bend with a curvature in the opposite direction compared to swelling.
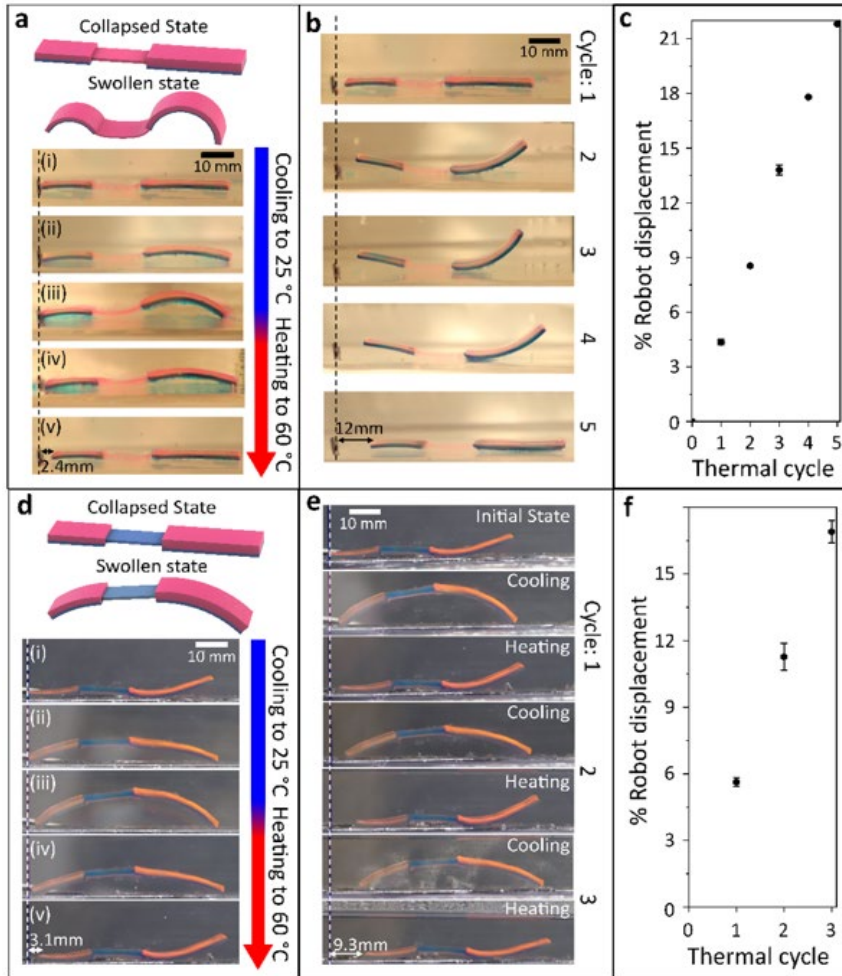
Figure 3. Thermal cycling of two versions of the two-segment robot. (a-c) With a flexible pNIPAM linker: (a) Experimental images of robot across one thermal cycle- The cooling half-cycle: **(i)** Cured state, **(ii)** Intermediate state, **(iii)** Swollen state. The heating half-cycle of the robot: **(iv)** Intermediate state, **(v)** Collapsed state of robot and displacement. **(b)** Experimental images of the robot observed at the end of each cycle of five complete thermal cycles. **(c)** Plot of the percentage robot displacement normalized by robot length over five cycles at the end of each thermal stimulation cycle. The robot crawls 12.0 mm in 5 cycles, i.e., 4.4 % body length/cycle. Here, body length is the cured state length of the robot ; **(d-f) With a stiff pAAM linker. (d)** Same as **(a). (e**) Experimental images of the robot observed at the end of each partial cycle (heating/cooling) of three complete thermal cycles. **(e)** Same as **(c)**, but for three cycles. The robot with the stiff linker crawls 9.3 mm in 3 cycles, i.e., 5.6 % body length/cycle. Bars in **(c)** and **(f)** indicate a standard deviation with a sample size of three.

The final curvature of the robot segments varied slightly with each cycle, likely due to differences

in the reorganization of the molecular chains of the crosslinked polymer and differences in

hydrogen bonding that occur between heating and cooling. (*40*) The two bilayers deswelled asynchronously from their swollen state curvature during this cycle. This deswelling was coupled with asymmetry in geometry and the rapid collapse of the middle segment and resulted in a forward translation of the robot (**Figure 3a**).

We subjected the robot to five thermal cycles, as shown in **Figure 3b**, and measured and plotted the displacement of the robot against each cycle. We observed that our robot crawled consistently in the direction of the larger bilayer, moving 4.4 % body length/cycle. We confirmed consistent unidirectional motion by performing a statistical study that involved stimulating the robot over 20 cycles of heating and cooling. (**Fig. S4c**)

Varying the morphology of the linker-two-segment robot with a stiff linker

We printed a second robot with the same bilayer specifications but replaced the original fully pNIPAM linker with a passive pAAM linker to investigate the design parameters that we can use to manipulate contact forces. We hypothesized that the stiffness of the linker would strongly influence the linker morphology and, consequently, the gait and contact forces of the robot. The robot was first thermally stimulated over three cycles, as shown in (**Figure 3d**). During the cooling half-cycle, the robot swelled up with the smaller bilayer curling more than the larger one, and the whole robot displaced minutely in either direction. However, the stiff linker held its shape and remained suspended between the bilayers. We observed that the smaller bilayer anchored as the larger bilayer leg deswelled during the heating cycle and displaced ahead by around (5.6 % body length/cycle) (**Movie S1**). Like our previous robots, we conducted a statistical study on the robot. We confirmed that our robot crawled consistently in the direction of the larger bilayer over 20 cycles of thermal stimulation (**Fig. S4d**).

Explaining the crawling mechanism using Finite Element Analysis

We obtained insight into our experimental findings by performing finite element analysis of the robot's behavior during thermal cycling. The constitutive model by Chester et al. assumed that the hydrogel was in a dry polymer state at the beginning of the simulation. (*39*) In contrast, the hydrogels are fabricated in a partially swollen state by direct ink writing. To achieve this initial swollen configuration, we simulated the free swelling of both the pNIPAM and pAAM materials at a reference temperature of 50 °C as described in the SI. The effects of gravity and buoyancy were prescribed by applying a body force, $b_y = \Delta \rho g$, where $\Delta \rho = 100$ kg/m^3 is the difference in the density between the polymer and water and g is gravitational acceleration. We discretized the bottom surfaces of all three segments of the robot (**Fig. S12**) using contact surface elements. We assumed a rigid surface underneath the segments with a Coulomb friction coefficient, $f_{\square} = 0.1$, to prevent interpenetration and to describe the frictional sliding of the robot during the temperature cycle.

We lowered the temperature from 50 °C to 25 °C at a rate of 1.67 °C/min and held it at 25°C for 2.45 hours, then heated it to 60 °C at 0.58 °C/min and held it at 60 °C for 2 hours, to simulate the actuation experiments. This caused the thermally responsive pNIPAM to swell during cooling and deswell during heating (**SI**). The swelling strain mismatch between the active pNIPAM and passive pAAM hydrogel caused the bilayer segments to curl downwards during cooling, pushing the pNIPAM linker into contact with the surface.
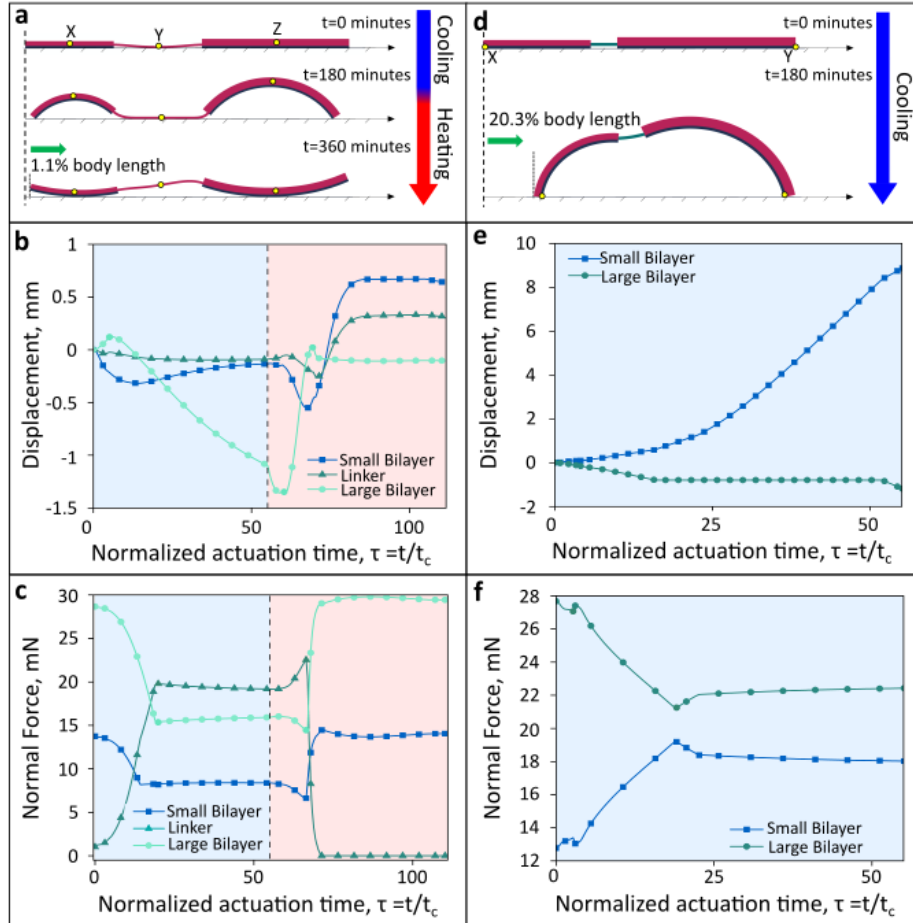
Figure 4. Finite element analysis of the two-segment robot. With a flexible linker: (a) Temporal snapshots of crawling upon cooling and heating. **(b)** A plot of the *x*-displacement of the center of the bilayers and the linker versus normalized time for cooling (blue area) and heating (red area) half-cycles. **(c)** A plot of the normal force exerted by different segments on the contact surface versus normalized time. **With a short and stiff linker: (d)** Temporal snapshots of smaller bilayer moving towards the larger bilayer upon cooling. **(e)** A plot of *x*-displacement of the outer edges of the bilayers versus normalized time. **(f)** A plot of the normal force on the contact surface exerted by the bilayers versus normalized time.

The left edge of the smaller bilayer moved to the right, and the right edge of the larger bilayer moved to the left (**Figure 4a**). The opposing motion of the bilayer segment resulted in a minimal 0.1 % translation of the center of the linker of the robot. The mismatch in the deswelling strain between pNIPAM and pAAM caused the robot to bend upward during heating. The bending of the

13

larger bilayer and deswelling of the linker pulled the robot to the right causing a net displacement of 1.1 % body length over the thermal cycle. (**Figure 4b**).

We plotted the normal force acting on the two bilayer segments and linker to understand the mechanism for forward translation of the hydrogel robot (**Figure 4c**). We calculated this by summing the nodal normal forces on the contact surface of an individual segment. The normal force scales with the magnitude of the friction force by the inverse of the Coulomb friction coefficient. Initially, the normal force was largest for the larger bilayer because it is the most massive segment in the robot. During cooling, the bending of the bilayers pushed on the linker, which caused it to experience the largest normal force and thus the largest friction force. The normal force acting on the bilayers decreased approximately by 50%. At the same time, the normal force increased by more than four times actor for the linker, which caused it to act as an anchor and the center of both bilayers to move towards the linker. Both bilayers first straightened and then curled upward, lifting the linker from the contact surface as we heated the robot to 60 °C. The larger bilayer was displaced by -0.1 mm during heating, while the smaller bilayer was displaced by 0.63 mm (**Figure 4a**). Once again, the larger bilayer experienced the largest friction force of the three segments and acted as an anchor, allowing the smaller bilayer and linker to slide to the right, producing a net forward motion **(Movie S2)**.

We performed two additional finite element simulations to validate the hypothesis for the mechanism of the robot locomotion. We changed the sequence of robot locomotion by changing the frictional anchoring of the robot. First, we switched the positions of the smaller and larger bilayers to produce net motion in the opposite direction. Having the larger bilayer on the left relocated the anchoring point during heating to the left and caused the smaller bilayer to slide to the left, producing a net motion to the left. The stroke (net motion) of the robot was the same in

magnitude ,but opposite in direction as the baseline case, and the friction force acting on the larger and smaller bilayers and the linker were the same as for the baseline case. We observed the same behavior in our experiments when we turned our flexible linker robot around and thermally stimulated it, and observed it crawl in the opposite direction (**Movie S3)**. We elaborate more on these studies in the SI (**Fig. S14**).

Next, we changed the design of the robot by replacing the pNIPAM linker with a passive hydrogel linker that was four times shorter than the original linker and three times stiffer than pAAM and simulated the motion during cooling (**Figure 4d**). The bending of the bilayers during cooling lifted the linker from the contact surface, creating an asymmetric arch.

The point of contact of the larger bilayer, point Y, was displaced by 2.1 %, while the point of contact of the smaller bilayer, point X, was displaced by a substantially larger amount, 20.3%, in the opposite direction (**Figure 4e**). The normal force was larger at point Y for the larger, more massive bilayer than at the contact point X for the smaller bilayer. This asymmetry in contact forces caused point Y to act as an anchor, and the robot translated to the right during the cooling period (**Figure 4f**). While we did not use a material of a similar stiffness ratio or bilayers of similar lengths, we observed the same trend of the robot displacing ahead by 7.6 % body length in our experiments when we switched our linker from a flexible pNIPAM to a stiff pAAM one (**Figure 3d**).
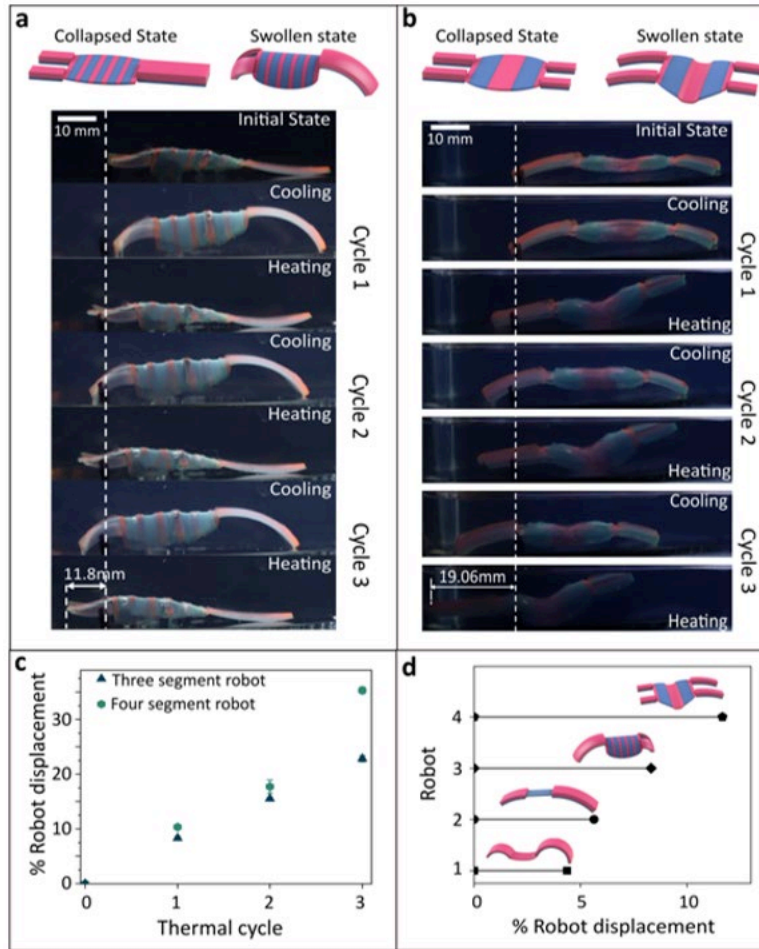
15

Figure 5- Robot displacement with varying bilayer segments and linker morphology: (a) Experimental images of the three-segment robot at the end of each heating and cooling half cycle over three consecutive cycles. **(b)** Experimental displacement of the robot over three thermal stimulation cycles. The robot moves 7.8 % body length/cycle. **(c)** Experimental images of the four-segment robot at the end of each heating and cooling half cycle over three consecutive cycles. **(d)** Experimental displacement of the robot over three thermal stimulation cycles. Robot moves 12.2 % body length/cycle.

Investigating the impact of the linker and bilayer morphology on robot gait

We characterized the morphology and displacement behavior of our gel robots by varying two additional factors, the linker pattern and the number of large/small bilayer segments. We redesigned the linker from the fully pNIPAM or pNIPAM composition described above and shown in **Figure 3** to a combination of alternating pAAM and pNIPAM strips, as shown in **Figure 5**. We also varied the number of large and small bilayer segments of the robots from two to three and four (**Figure 5**). We stimulated our robots across multiple thermal cycles, and the results are discussed below.

Three-segment robot with a striped linker

This gel robot depicted in **Fig. S5a** consisted of two small and one large bilayer segment connected by a linker composed of five strips of pAAM and six stripes of pNIPAM. Like the previous gel robots consisting of one small and one large bilayer segment connected by a uniform linker, we observed that the two smaller bilayers achieved different curvatures in the swelling cycle and equilibrated faster than the larger bilayer. This asymmetry in the morphology of the bilayers resulted in the robot undergoing minimal unidirectional translation at the end of the cooling half-cycle. We observed that the linker sagged a bit, barely touching the surface because of pNIPAM swelling; the pAAM strips maintained the mechanical integrity of the linker (**Figure 5a**). After reaching equilibrium, we switched the temperature for the heating cycle. We observed a stick-slip motion due to uneven contact forces between the larger and smaller bilayer segments that caused a larger displacement within the 5-minute interval.

Further heating resulted in pNIPAM deswelling beyond its cured state length and caused the bilayers to bend with a negative curvature compared to that during swelling. We thermally stimulated our robot initially for three cycles, as shown in **Figure 5b**, and measured and plotted

the displacement of the robot against each cycle. Our robot crawls unidirectionally with approximately 7.8 % body length/cycle displacement towards its smaller bilayer (**Movie S4**). We also performed a statistical study on this gel robot over 20 cycles to confirm consistent unidirectional motion (**Fig. S5c**) and compared its displacement to a similar bilayer segment robot with a flexible pNIPAM linker (Three-segment robot with a flexible pNIPAM linker) (**Fig. S6**). These studies confirm that the contact force is distributed differently from the three-segment robot with an alternating linker because the linker sags and touches the surface excessively. The two ends of the robot have less asymmetry, which causes the displacement to reduce the robot locomotes the only 3.9. % (**Movie S5**).

Four-segment robot with a striped linker

This gel robot depicted in **Fig. S5b** consisted of two small and two large bilayers segments connected by a linker composed of two strips of pAAM and three strips of pNIPAM. We observed that the smaller bilayers deswelled and lifted from the surface during the heating half-cycle, the larger bilayers staying anchored at the starting point. As the gel robot swelled during the cooling half-cycle, the asymmetric deswelling of the two pairs of bilayers caused the smaller pair of bilayers to bend and anchor on the surface. At the same time, the expanding pNIPAM in the linker pushed the now unanchored, larger bilayers ahead, displacing the robot by 12.2 % body length/cycle (**Figure 5c, Movie S6**). We confirmed consistent unidirectional motion towards the larger bilayer by conducting a 20-cycle statistical study on our robot like our previous robots. Importantly, we observe a trend in that the displacement increases with increasing asymmetry in contact forces, which we can tune by varying the linker morphology and bilayer segments (**Fig. S5d).**

DISCUSSION

We describe and validate a new mechanism for untethered unidirectional crawling for multisegmented gel robots on flat unpatterned substrates. The mechanism relies on a spatial morphological gradient along the fore-aft axis that in turn leads to temporal asymmetry and, ultimately, asymmetry in contact forces of gel segments and linkers, leading to unidirectional locomotion. Using a model gel robot consisting of two bilayer segments with either a stiff or flexible linker, we investigate the mechanism experimentally by thermal cycling and compare the results to FEA simulations. These studies help us calculate the asymmetry of the contact forces during swelling and deswelling half-cycles in different parts of the gel robot, which drive asymmetry in anchoring and release of the segments to produce a net displacement. We also demonstrate that we can tune and increase the magnitude of the displacement by varying linker morphology and the number of bilayer segments. We believe that exploiting morphology to tune distributed spatiotemporal dynamics of soft robots holds promise for the next generation of autonomous shape-changing devices and chemo-bio-thermo-mechanical soft locomotor robots.

MATERIALS AND METHODS

Ink preparation

We formulated hydrogel inks compatible with the DIW 4D printing process mentioned in **Figure 1a** by modifying the rheological properties of our inks to make them shear thinning. We used the nano clay Laponite® as a rheology modifier for this purpose. (*10*) We used acrylamide (AAM) for the passive ink and N-isopropylacrylamide (NIPAM) for the active ink. We prepared a sacrificial ink with only Laponite® and water to print the supporting layer.

We blended Laponite® XLG (BYK USA Inc.) with deionized (DI) water, a 0.12 mg/mL solution of methacryloxyethyl thiocarbamoyl rhodamine B (Polysciences, Inc.) dye solution for the active ink. We homogenized it in the planetary mixer (Mazerustar KK-250S, Kurabo Industry Ltd.). We used a 0.5 mg/mL solution of methylene blue (Sigma Aldrich) dye for the passive ink for macro imaging. After this, we added the NIPAM monomer (Scientific Polymer Products Inc.) and the UV photoinitiator Irgacure 2959 (BASF) to the Laponite® solution for the active ink. For the passive ink, we added AAM monomer (Sigma-Aldrich), Irgacure 2959, and the crosslinker N, N′-methylenebisacrylamide (BIS, Sigma-Aldrich) to the Laponite® solution. Final concentrations of the inks were: Active Ink- (DI water-84.6 %; NIPAM-8.5 %; Laponite® -6.8 %; Irgacure-0.2) and Passive Ink- (DI water-83 %; AAM-7.9 %; Laponite® -6.6 %; Irgacure-0.8; BIS-1.7 %). We homogenized the inks again in the planetary mixer. We made the sacrificial ink by homogenizing an 8 % solution of Laponite®. We let all our inks age for a day for the desired rheological properties. We show the microstructures of the ink in **Fig. S1b**.

Bilayer transient actuation study

After curing, we placed each group of samples in a 20 cm x 10 cm clear plastic box. We added 750 mL of DI water at room temperature to the box and used a broad-spectrum UV light source to excite the fluorescent dye in the structures. We observed each group for over 8 hours. After the bilayers were at equilibrium at 25 °C, we heated it to 60 °C at 1.75 °C/min and imaged it with a DSLR camera (Canon).

Finite element analysis

We used finite element analysis to investigate the crawling mechanism of the two-segment robot with a flexible linker. We applied the thermo-chemo-mechanical model of thermoresponsive hydrogels by Chester et al. (*39*), implemented as a user-defined element (UEL) subroutine in

ABAQUS, to describe the coupled thermo-chemo-mechanical behavior of the pNIPAM and pAAM hydrogels. (*41*) Additional details of the constitutive model and its implementation can be found in (**SI**).

Briefly, the model assumes an additive decomposition of the free energy density constituted of a mechanical part, described by the compressible Neo-Hookean potential, and a mixing part given by the Flory-Huggins potential. (*42*) Further, to describe the stress-coupled transport of water into the hydrogel, Chester et al. (*39*) also assume a linear constitutive relationship between the fluid flux and gradient of chemical potential while the balance law for fluid content takes large deformation into account. Performing 3D finite simulations of coupled thermo-chemo-mechanical problems is computationally expensive; thus, we performed 2D plane-strain finite element simulations. The model contains seven parameters: the shear modulus, bulk modulus, temperature-dependent Flory-Huggins interaction parameters, swelling and deswelling diffusivities, the atomic volume of solvent, and reference chemical potential. We have listed the material parameters for both hydrogels in **Table S2 and S3**. We obtained the shear moduli of the hydrogels from rheological characterizations done in a previous study. (*10*)

Thermal cycling of robots

After curing and sacrificial layer dissolution, we thermally cycled the robots in water on a hot plate (Thermofisher) by switching the temperature to 60 °C for the heating half-cycle and back to 25 °C for the cooling half-cycle. We generated all the figures in the main text using a three or five cycle on our robots. For the statistical study of robot displacement shown in **Fig. S4-6**, we stimulated the robots over ten thermal cycles, turned them around, and stimulated it for ten more thermal cycles. All our robot crawling studies were done on silicon wafers and in triplicate.

References and Notes

1. L. Ricotti, B. Trimmer, A. W. Feinberg, R. Raman, K. K. Parker, R. Bashir, M. Sitti, S. Martel, P. Dario, A. Menciassi, Biohybrid actuators for robotics: A review of devices actuated by living cells. Sci Robot. 2, (2017). doi:10.1126/scirobotics.aaq0495

2. M Cianchetti, C. Laschi, A. Menciassi, P. Dario, Biomedical applications of soft robotics. Nat. Rev. Mater. 3, 143–153 (2018). doi: 10.1038/s41578-018-0022-y

3. O. Erol, A. Pantula, W. Liu, D. H. Gracias, Transformer Hydrogels: A Review. Adv. Mater. Technol. 4, 1900043 (2019). doi: 10.1002/admt.201900043

4. L. Hines, K. Petersen, G. Z. Lum, M. Sitti, Soft Actuators for Small-Scale Robotics. Adv. Mater. 29, (2017). doi:10.1002/adma.201603483

5. M. A. C. Stuart, W. T. S. Huck, J. Genzer, M. Müller, C. Ober, M. Stamm, G. B. Sukhorukov, I. Szleifer, V. V. Tsukruk, M. Urban, F. Winnik, S. Zauscher, I. Luzinov, S. Minko, Emerging applications of stimuli-responsive polymer materials. Nat. Mater. 9, 101–113 (2010). doi: 10.1038/nmat2614

6. X. Liu, J. Liu, S. Lin, X. Zhao, Hydrogel machines. Mater. Today. 36, 102–124 (2020). doi: 10.1016/j.mattod.2019.12.026

7. L. Tan, A. C. Davis, D. J. Cappelleri, Smart polymers for microscale machines. Adv. Funct. Mater. 31, 2007125 (2021). doi:10.1002/adfm.202007125

8. T.-Y. Huang, H. Gu, B. J. Nelson, Increasingly Intelligent Micromachines. Annu. Rev. Control Robot. Auton. Syst. 5, 279-310 (2022). doi: 10.1146/annurev-control-042920-013322.

9. H. Yuk, S. Lin, C. Ma, M. Takaffoli, N. X. Fang, X. Zhao, Hydraulic hydrogel actuators and robots optically and sonically camouflaged in water. Nat. Commun. 8, 14230 (2017). doi: 10.1038/ncomms14230

10. J. Liu, O. Erol, A. Pantula, W. Liu, Z. Jiang, K. Kobayashi, D. Chatterjee, N. Hibino, L. H. Romer, S. H. Kang, T. D. Nguyen, D. H. Gracias, Dual-Gel 4D Printing of Bioinspired Tubes. ACS Appl. Mater. Interfaces. 11, 8492–8498 (2019). doi: 10.1021/acsami.8b17218

11. M. Li, A. Pal, A. Aghakhani, A. Pena-Francesch, M. Sitti, Soft actuators for real-world applications. Nat. Rev. Mate 1–15 (2021). doi: 10.1038/s41578-021-00389-7

12. K. Jain, R. Vedarajan, M. Watanabe, M. Ishikiriyama, N. Matsumi, Tunable LCST behavior of poly(N-isopropylacrylamide/ionic liquid) copolymers. Polym. Chem. 6, 6819–6825 (2015). doi: 10.1039/C5PY00998G

13. K. Kobayashi, S. H. Oh, C. Yoon, D. H. Gracias, Multitemperature Responsive Self-Folding Soft Biomimetic Structures. Macromol. Rapid Commun. 39, (2018). doi:10.1002/marc.201700692.

14. S. Maeda, Y. Hara, T. Sakai, R. Yoshida, S. Hashimoto, Self-Walking Gel. Advanced Materials. 19 (2007), pp. 3480–3484. doi: 10.1002/adma.200700625

15. H. Arora, R. Malik, L. Yeghiazarian, C. Cohen, U. Wiesner, Earthworm inspired locomotive motion from fast swelling hybrid hydrogels. Journal of Polymer Science Part A: Polymer Chemistry. 47 (2009), pp. 5027–5033. doi: 10.1002/pola.23555

16. J. Kim, S. E. Chung, S.-E. Choi, H. Lee, J. Kim, S. Kwon, Programming magnetic anisotropy in polymeric microactuators. Nat. Mater. 10, 747–752 (2011). doi: 10.1038/nmat3090

17. F. Vernerey, T. Shen, The mechanics of hydrogel crawlers in confined environment. J. R. Soc. Interface. 14 (2017), doi:10.1098/rsif.2017.0242. doi: 10.1098/rsif.2017.0242

18. T. Shen, M. G. Font, S. Jung, M. L. Gabriel, M. P. Stoykovich, F. J. Vernerey, Remotely Triggered Locomotion of Hydrogel Mag-bots in Confined Spaces. Sci. Rep. 7, 16178 (2017). doi: 10.1038/s41598-017-16265-w

19. G. Gao, Z. Wang, D. Xu, L. Wang, T. Xu, H. Zhang, J. Chen, J. Fu, Snap-Buckling Motivated Controllable Jumping of Thermo-Responsive Hydrogel Bilayers. ACS Appl. Mater. Interfaces. 10, 41724–41731 (2018). doi: 10.1021/acsami.8b16402

20. A. S. Gladman, E. A. Matsumoto, R. G. Nuzzo, L. Mahadevan, J. A. Lewis, Biomimetic 4D printing. Nat. Mater. 15, 413–418 (2016). doi: 10.1038/nmat4544

21. S. E. Bakarich, R. Gorkin, S. Naficy, R. Gately, M. in H. Panhuis, G. M. Spinks, 3D/4D Printing Hydrogel Composites: A Pathway to Functional Devices. MRS Advances. 1, 521–526 (2016). doi: 10.1557/adv.2015.9

22. Y. Mao, Z. Ding, C. Yuan, S. Ai, M. Isakov, J. Wu, T. Wang, M. L. Dunn, H. J. Qi, 3D Printed Reversible Shape Changing Components with Stimuli Responsive Materials. Sci. Rep. 6, 24761 (2016). doi: 10.1038/srep24761

23. Q. Ge, A. H. Sakhaei, H. Lee, C. K. Dunn, N. X. Fang, M. L. Dunn, Multimaterial 4D Printing with Tailorable Shape Memory Polymers. Sci. Rep. 6, 31110 (2016). doi: 10.1038/srep31110

24. N. Wang, X. Ge, H. Guo, C. Cui, X. Zhang, A kind of soft pneumatic actuator based on multi-material 3D print technology. 2017 IEEE International Conference on Robotics and Biomimetics (ROBIO) (2017), , doi:10.1109/robio.2017.8324519. doi: 10.1109/ROBIO.2017.8324519

25. Y. Jin, Y. Shen, J. Yin, J. Qian, Y. Huang, Nanoclay-Based Self-Supporting Responsive Nanocomposite Hydrogels for Printing Applications. ACS Appl. Mater. Interfaces. 10, 10461–10470 (2018). doi: doi.org/10.1021/acsami.8b00806

26. M. Schaffner, J. A. Faber, L. Pianegonda, P. A. Rühs, F. Coulter, A. R. Studart, 3D printing of robotic soft actuators with programmable bioinspired architectures. Nat. Commun. 9, 878 (2018). doi: 10.1038/s41467-018-03216-w

27. J. Guo, R. Zhang, L. Zhang, X. Cao, 4D Printing of Robust Hydrogels Consisted of Agarose Nanofibers and Polyacrylamide. ACS Macro Lett. 7, 442–446 (2018). doi: 10.1021/acsmacrolett.7b00957

28. J. Liu, W. Liu, A. Pantula, Z. Wang, D. H. Gracias, T. D. Nguyen, Periodic buckling of soft 3D printed bioinspired tubes. Extreme Mechanics Letters. 30, 100514 (2019). doi: 10.1016/j.eml.2019.100514

29. S. Kuroda, I. Kunita, Y. Tanaka, A. Ishiguro, R. Kobayashi, T. Nakagaki, Common mechanics of mode switching in locomotion of limbless and legged animals. J. R. Soc. Interface. 11, 20140205 (2014). doi: 10.1098/rsif.2014.0205

30. E. R. Trueman, The Locomotion of Soft-bodied Animals (Edward Arnold, 1975). doi: 10.1086/409544

31. R. D. Maladen, Y. Ding, C. Li, D. I. Goldman, Undulatory swimming in sand: subsurface locomotion of the sandfish lizard. Science. 325, 314–318 (2009). doi: 10.1126/science.1172490

32. Y. Tanaka, K. Ito, T. Nakagaki, R. Kobayashi, Mechanics of peristaltic locomotion and role of anchoring. J. R. Soc. Interface. 9, 222–233 (2012). doi: 10.1098/rsif.2011.0339

33. J. Aguilar, T. Zhang, F. Qian, M. Kingsbury, B. McInroe, N. Mazouchova, C. Li, R. Maladen, C. Gong, M. Travers, R. L. Hatton, H. Choset, P. B. Umbanhowar, D. I. Goldman, A review on locomotion robophysics: the study of movement at the intersection of robotics, soft matter and dynamical systems. Rep. Prog. Phys. 79, 110001 (2016). doi: 10.1088/0034-4885/79/11/110001

34. S. Hirose, H. Yamada, Snake-like robots [Tutorial]. IEEE Robot. Autom. Mag. 16, 88–98 (2009). doi: 10.1109/MRA.2009.932130

35. C. Wright, A. Johnson, A. Peck, Z. McCord, A. Naaktgeboren, P. Gianfortoni, M. Gonzalez-Rivero, R. Hatton, H. Choset, in 2007 IEEE/RSJ International Conference on Intelligent Robots and Systems (2007), pp. 2609–2614. doi: 10.1109/IROS.2007.4399617

36. C. Wright, A. Buchan, B. Brown, J. Geist, M. Schwerin, D. Rollinson, M. Tesch, H. Choset, in 2012 IEEE International Conference on Robotics and Automation (2012), pp. 4347–4354. doi: 10.1109/ICRA.2012.6225255

37. J. Liu, O. Erol, A. Pantula, W. Liu, Z. Jiang, K. Kobayashi, D. Chatterjee, N. Hibino, L. H. Romer, S. H. Kang, T. D. Nguyen, D. H. Gracias, Dual-Gel 4D Printing of Bioinspired Tubes. ACS Applied Materials & Interfaces. 11 (2019), pp. 8492–8498. doi: 10.1021/acsami.8b17218

38. T. Tanaka, E. Sato, Y. Hirokawa, S. Hirotsu, J. Peetermans, Critical kinetics of volume phase transition of gels. Phys. Rev. Lett. 55, 2455–2458 (1985). doi: 10.1103/PhysRevLett.55.2455

39. S. A. Chester, L. Anand, A thermo-mechanically coupled theory for fluid permeation in elastomeric materials: Application to thermally responsive gels. J. Mech. Phys. Solids. 59, 1978–2006 (2011). doi: 10.1016/j.jmps.2011.07.005

40. Y. Lu, K. Zhou, Y. Ding, G. Zhang, C. Wu, Origin of hysteresis observed in association and dissociation of polymer chains in water. Phys. Chem. Chem. Phys. 12, 3188–3194 (2010). doi: 10.1039/B918969F

41. S. A. Chester, C. V. Di Leo, L. Anand, A finite element implementation of a coupled diffusion-deformation theory for elastomeric gels. Int. J. Solids Struct. 52, 1–18 (2015). doi: 10.1016/j.ijsolstr.2014.08.015

42. P. J. Flory, Thermodynamics of High Polymer Solutions. J. Chem. Phys. 10, 51–61 (1942). 10.1063/1.1723621

43. D. Bonn, S. Tanase, B. Abou, H. Tanaka, J. Meunier, Laponite: aging and shear rejuvenation of a colloidal glass. Phys. Rev. Lett. 89, 015701 (2002). doi: 10.1103/PhysRevLett.89.015701

44. C. Love, E. D. Rainville. Differential and Integral Calculus. Sixth Edition (Macmillan Company, 1962).

45. W. Hong, X. Zhao, J. Zhou, Z. Suo, A theory of coupled diffusion and large deformation in polymeric gels. J. Mech. Phys. Solids. 56, 1779–1793 (2008). doi: 10.1016/j.jmps.2007.11.010

46. S. A. Chester, L. Anand, A coupled theory of fluid permeation and large deformations for elastomeric materials. J. Mech. Phys. Solids. 58, 1879–1906 (2010). doi: 10.1016/j.jmps.2010.07.020